NUMERICAL SIMULATION OF M9 MEGATHRUST EARTHQUAKES IN THE CASCADIA SUBDUCTION ZONE

D. ROTEN[1], K.B. OLSEN[1] and R. TAKEDATSU[1]

[1]San Diego State University, San Diego, CA, United States

E-mail contact of main author: daniel.roten@mail.sdsu.edu

Abstract. We estimate ground motions in the Pacific Northwest urban areas during M9 subduction scenario earthquakes on the Cascadia megathrust by simulating wave propagation from an ensemble of kinematic source descriptions. Velocities and densities in our computational mesh are defined by integrating the regional Cascadia Community Velocity Model (CVM) v1.6 [1] including the ocean water layer with a local velocity model of the Georgia and Seattle basins [2], including additional near-surface velocity information. We generate six source realizations, each consisting of a background slip distribution with correlation lengths, rise times and rupture velocities consistent with data from previous megathrust earthquakes (e.g., 2011 M 9 Tohoku or 2010 M 8.8 Maule). We then superimpose M~8 subevents, characterized by short rise times and high stress drops on the background slip model to mimic high-frequency strong ground motion generation areas in the deeper portion of the rupture [3]. The wave propagation is simulated using the discontinuous mesh (DM) version of the AWP finite difference code. We simulate frequencies up to 1.25 Hz, using a spatial discretization of 100 m in the fine grid, resulting in surface grid dimensions of 6,540 x 10,728 mesh points. At depths below 8 km, the grid step increases to 300 m. We obtain stable and accurate results for the DM method throughout the simulation time of 7.5 mins as verified against a solution obtained with a uniform 100 m grid spacing. Peak ground velocities (PGVs) range between 72 and 100 cm/s in downtown Seattle and between 25 and 54 cm/s in downtown Vancouver, while spectral accelerations at 2 s range between 1.7 and 3.6 m/s^2 and 1.0 and 1.3 m/s^2, respectively. These long-period ground motions are not significantly reduced if plastic Drucker-Prager yielding in shallow cohesionless sediments is taken into account. Effects of rupture directivity are significant at periods of ~10 seconds, but almost absent at shorter periods. We find that increasing the depth extent of the subducting slab from the truncation at 60 km in the Cascadia CVM version 1.6 to ~100 km increases the PGVs by 15% in Seattle.

Key Words: Long-period ground motion, wave propagation simulation, megathrust earthquake, finite difference method.

1. Introduction

The Cascadia subduction zone, which extends from the Mendocino Triple Junction northwards to Vancouver Island, marks the ~1,000 km long boundary between the Juan de Fuca (JdF) plate to the West and the North American (NA) plate to the East (FIG. 1). The paleoseismic record shows that the Cascadia subduction zone has repeatedly produced large megathrust earthquakes (M > 8) with a recurrence period of approximately 500 years [4]. The last M9 Cascadia earthquake which occurred in 1700 A.D. is well documented from native stories, Japanese records and radiocarbon tree-ring dating [5]. A Cascadia megathrust earthquake represents a major source of seismic hazard to the Pacific Northwest, in particular to the large metropolitan areas of Seattle (population 3.8M), Vancouver (population 2.5M) and Portland (population 2.4M) which are located on top of deep sedimentary basins that could further amplify the seismic waves [6, 7].

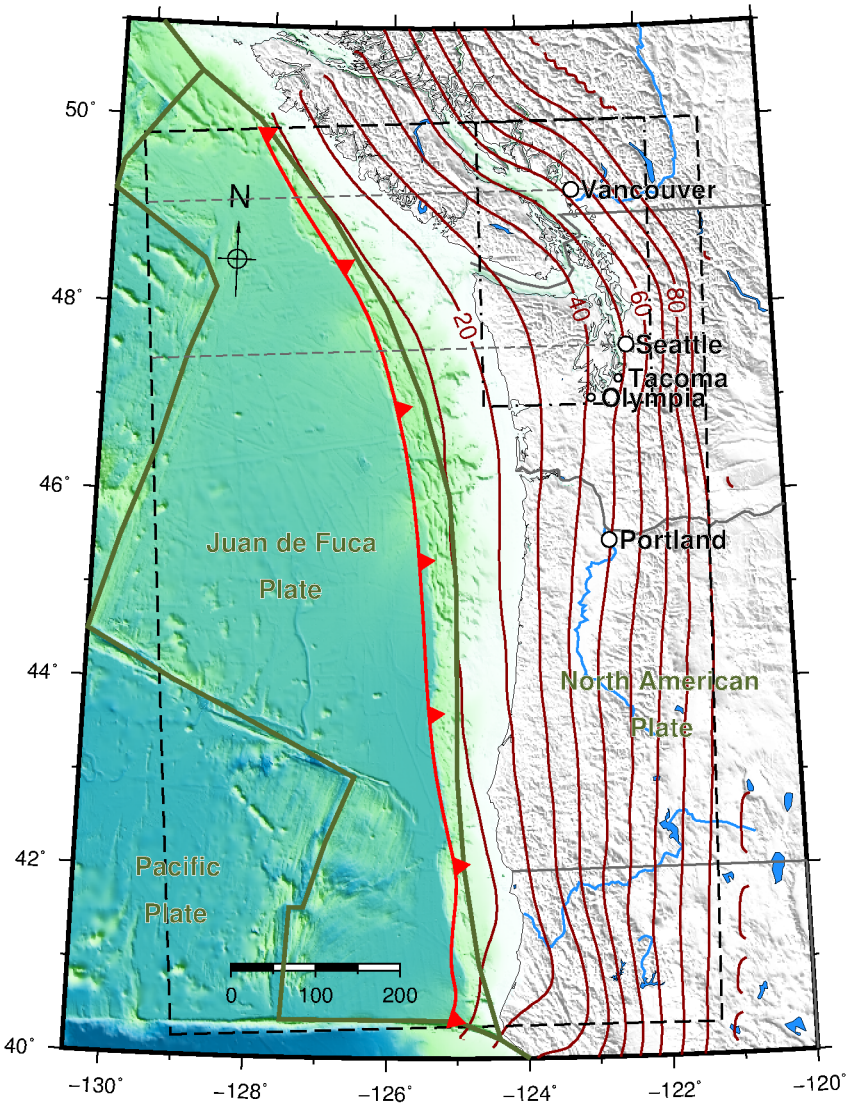

FIG. 1. Plate boundaries (dark green lines) in the Cascadia area and oceanic trench (thick solid red line). The dashed rectangle outlines the extent of the computational domain; the dash-dotted inner rectangle shows the extent of the Georgia basin CVM. Red contours show the depth of the subduction slab (in km, from [8, 9]). Dashed gray (E-W) lines depict profiles along which cross-sections are shown in FIG. 2.

Because no Cascadia megathrust earthquake has occurred since the onset of instrumental seismology, numerical simulations of wave propagation represent our best option to estimate the level of ground motion to be expected during the next such event. The first 3D simulations of a M9 Cascadia megathrust earthquake by Olsen *et al*. [10] used a long-period ($f < 0.5$ Hz) source model obtained by mapping slip inversion results of the M_w 9.1—9.3 Sumatra—Andaman earthquake [11] onto the Cascadia subduction slab. Olsen *et al*. [10] also introduced a community velocity model (CVM) for the Pacific Northwest [12] which incorporates continental and oceanic sedimentary basin, crust and mantle units. The 3D simulations predicted peak ground velocities of up to 42 cm/s and shaking durations of up to 5 minutes in the Seattle area, which would represent a significant threat to high-rise buildings [10].

More recently, Molnar *et al*. [2, 13] developed a refined version of the CVM for the Georgia basin region by including shallow (< 1 km) high-resolution velocity information from geologic maps, P-wave tomography, boreholes and seismic surveys. Molnar *et al*. simulated a total of

10 deep JdF plate earthquakes, including the 2001 M 6.8 Nisqually earthquake, and found that the updated velocity model reproduces PGVs observed in the Vancouver area more accurately than the base Pacific Northwest CVM.

Both previous simulations efforts [10, 13] used a spatial discretization of 250 m and a minimum shear-wave velocity of 625 m/s, restricting the frequency content of synthetic ground motions that can be accurately predicted to less or equal 0.5 Hz. This limitation reduces the usability of deterministic simulations for the purpose of predicting building response, as the frequency band of engineering interest extends to at least 10 Hz. Here, we present higher-resolution (Δh = 100 m) simulation results for M9 Cascadia megathrust earthquakes, where deterministic ground motions are predicted for a maximum frequency of 1.25 Hz. These long-period ground motions will be complemented with a high-frequency component to produce broadband (0—10 Hz) synthetics.

2. Computational Model Domain

The computational domain includes the entire region covered by the Cascadia CVM and stretches from 40.2°N to 50°N latitude and from 129°W to 122°W longitude (FIG. 1). P-wave velocities, S-wave velocities and densities were adopted from version 1.6 of the CVM [1]. P-wave velocities in the Cascadia CVM are based on available data for the continental crust and mantle and for the oceanic units, with S-wave velocities and densities derived from P-wave velocities using an empirical relationship [14]. Inside continental sediments, both P- and S-wave velocities are derived from geological and geophysical information about the Quaternary and Tertiary deposits, including borehole data, seismic surveys and V_{S30} measurements. The Cascadia subduction interface is modeled after data from earthquake locations and seismic velocity studies [8, 9]. We obtained the Cascadia CVM in 500 m resolution and resampled it to 100 m resolution using linear interpolation.

Inside the Georgia basin and Puget Sound regions (dash-dotted rectangle in *FIG. 1*), we adopted material properties from the refined version of the Cascadia CVM [13] (thereafter referred to as Georgia basin CVM), which is available in 250 m resolution. In order to avoid sharp contrasts at the intersection between the Cascadia CVM version 1.6 and the Georgia basin CVM, we defined a 20 km wide transition zone in which material properties of the two CVMs are gradually weighted using a ramp taper. At depths below 5 km, the Cascadia CVM version 1.6 was always used. *FIG. 2* shows shear-wave velocities along two profiles through Vancouver and Seattle, respectively.

Along the vertical direction, the Cascadia CVM includes the region between mean sea level (0 km) and 60 km depth [1], which is relatively shallow with respect to the horizontal extent. However, the top of the subducted slab is deeper than 60 km in the NE corner of the domain (FIG. **1**). To investigate the effect of the deeper slab geometry on ground motions in the Vancouver and Seattle areas, we extended the Cascadia CVM to 120 km depth. We used the 3-D geometry of the subducted JdF plate for the region [8] and assigned the Cascadia CVM properties for oceanic mantle to volumes below the slab and deeper than 60 km (FIG. 2). Inside regions located above the slab but below 60 km depth, shear-wave velocities were extracted from a 3-D tomography model of the western United States [15], which also provides P-wave velocities and densities based on empirical relationships. We included the ocean water layer defined by v_p = 1500 m/s, v_s = 0, and density ϱ = 1,025 kg/m3, incorporated above the sea bottom interface defined within the Cascadia CVM.

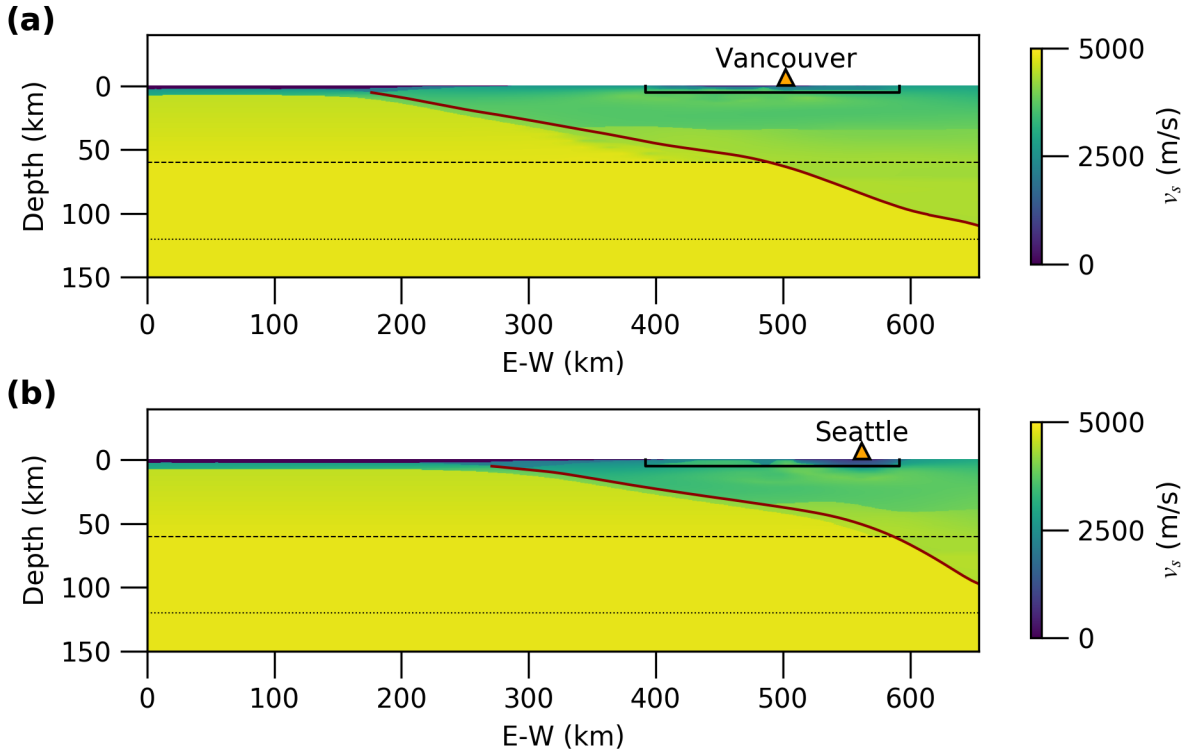

FIG. 2. Vertical cross-sections (see locations in FIG. 1) of shear-wave velocity v_s along profiles from West to East through (a) Vancouver and (b) Seattle (triangles). The solid dark red line shows the upper slab surface [8, 9]. Horizontal dashed and dotted lines show the vertical extent of the 60 and 120 km deep models, respectively. The black solid line marks the extent of the Georgia basin CVM [13].

3. Kinematic Source Realizations

Near-source strong motion observations made during the 2010 M_w 8.8 Maule, Chile and the 2011 M_w 9—9.1 Tohoku earthquake have significantly improved our understanding of the rupture process pertaining to great (M > 8.5) subduction zone interface earthquakes. The rupture process of both earthquakes exhibited variations in the predominant frequency of radiation as a function of depth. In particular, low-frequency (~0.2 Hz) energy was radiated from shallow regions close to the trench, and short-period (~1 Hz) energy was emitted from deeper areas of the subducting slab [16, 17].

In the case of the Tohoku earthquake, two major slip events with long rise time (~40 s) occurred at shallow depths close to the trench [18]. This background slip, which produced up to 60 m of displacement that triggered the destructive tsunami [19], was well resolved from inversion of local and teleseismic records [20] and long-period back-projections [21]. On the other hand, back-projections of short-period teleseismic P-waves located the source below the Honshu coastline [16, 22, 23]. Long-period inversions of teleseismic arrivals from the Maule earthquake identify most of the slip to the north and south (up-dip) of the hypocenter [24], while back-projections of P-waves trace the origin of high-frequency energy to roughly the same depth as the hypocenter (~35 km).

Because the short-period ($f > 0.1$ Hz) waves emitted from the deeper part are mainly relevant for engineering, efforts to predict ground motions from large megathrust earthquakes must take the frequency-dependence nature of such events into account. Frankel [3] modeled the 2010 Maule earthquake using a kinematic rupture model, which consisted of a background slip

distribution with long rise times and superimposed high stress-drop asperities with short rise times, and obtained a good match between simulated and observed spectral accelerations. Kurashashi and Irikura [25, 26] created a short-period source model of the 2011 Tohoku earthquake which consisted of 5 subevents identified as strong motion generation areas, and generated synthetic ground motions using the empirical Green's function method. Galvez & Dalguer [27] introduced a dynamic rupture model of the Tohoku earthquake which involved rupture reactivation on the main near-trench slip area connected to a second large slip area by deeper, small asperities with high stress drop.

For the M9 Cascadia simulations presented here, we create a suite of compound kinematic source models using a similar method as Frankel [3]. The background slip distribution was generated using a von Karman autocorrelation function. Because empirical relationships for stochastic characterizations of earthquake slip are only available for crustal earthquakes [28], autocorrelation distances were manually chosen to obtain a rough visual agreement with slip inversion results [3, 29] (100 km ≤ $a_{x,z}$ ≤ 1,000 km), and the Hurst coefficient was set to 0.75. At the edges of the rupture surface, slip was gradually tapered to zero within a 200—300 km wide area bound by two concentric ellipses to avoid a box-like appearance of the final slip distribution.

In order to map the planar slip distribution onto the irregular fault geometry [30], we created a grid of along-strike and along-dip distances on the 3-D representation of the subducting slab surface [8]. First, along-strike and along-dip distances were computed on iso-depth contours of the slab surface, with strike distances tracked along the contour and dip distances computed in the direction perpendicular to the contours. Next the corresponding strike and dip position of each subfault was established from the contour values (*FIG. 3a*) by linear interpolation. The strike and dip positions on the curved slab were then used to interpolate rupture parameters defined on a planar fault for each subfault in the finite difference grid. FIG. 3b shows the background slip on the irregular fault obtained from rupture model A.

The slip distribution of the subevents was also generated using a von Karman autocorrelation function, but with shorter autocorrelation lengths of 50 km [28]. The subevents cover a circular area of about 100 km diameter each, with the subevent magnitude ranging from 7.9 to 8.1. The five subevents were placed at along-dip distances between 60 and 120 km, which puts them at depths of ~20 km near the center of the transition zone (FIG. 3c), shallower than the 30—40 km depth identified for subevents or strong motion generation areas in studies of the Tohoku earthquake [18, 26]. To analyze the impact of subevent depth on ground motions, we also performed one simulation with the subevents moved further to the east, at depths between 25 and 30 km (rupture model A'). The total slip of each rupture scenario was obtained by superimposing the five subevents on the background slip model (FIG. 3d), resulting in a total event magnitude between 9 and 9.1.

Following Frankel [3], we computed rupture initialization times for each subfault using the distance from the subfault to the hypocenter, x_i, and the secant rupture velocity associated with that subfault, v_{ri},

$$t_i = {}^{x_i}/_{v_{ri}} + \sigma_i,$$

with the random value σ_i chosen from a uniform distribution between ±0.4 s. The secant rupture velocity v_{ri} is derived from an assumed average rupture velocity $\bar{v}_r$ and a perturbation reflecting the difference between total local slip u_i and average slip $\bar{u}$ [3]:

$$v_{ri} = \bar{v}_r + c(u_i - \bar{u}).$$

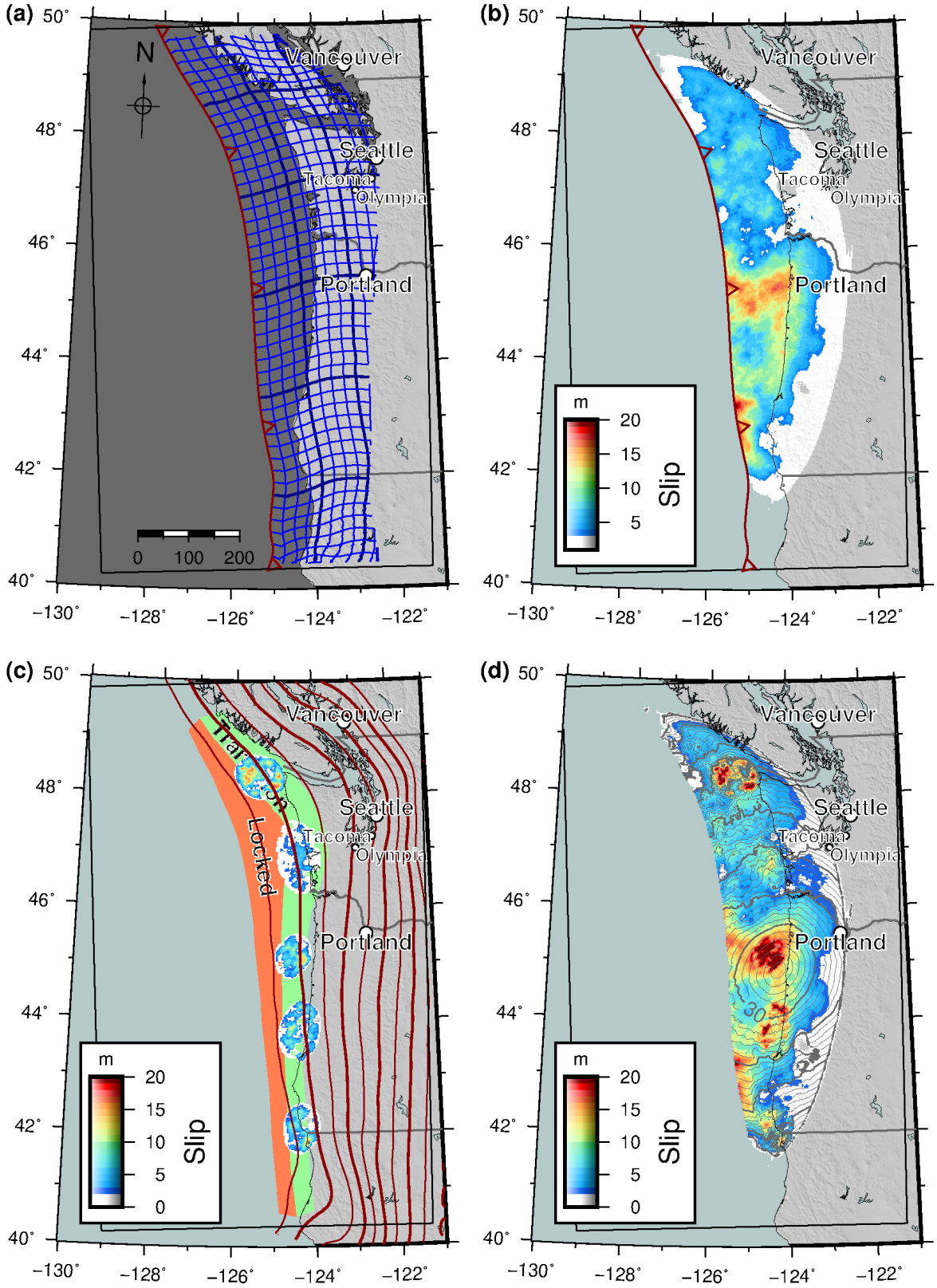

FIG. 3. Surface projection of the megathrust rupture. (a) Fault surface with 25 km contours of along-strike and along-dip distances. (b) M 9.1 background slip and (c) M 7.9—8.1 subevents, including extent of locked (orange) and transition (light green) zones on the subducting slab from [31]) (d) Compound slip in rupture model A, with solid gray contours showing rupture times in 5 s intervals.

The constant *c* is determined by specifying a standard deviation of 10%, and the average rupture velocity is set to 2,500 m/s [3]. This definition results in slightly higher rupture velocities in areas of higher slip, which is consistent with findings from dynamic rupture simulations [32].

The rise time of each subfault was obtained by dividing the total slip by the slip velocity. We adopted background and subevent slip velocities of 1.3 m/s and 5.4 m/s, respectively, from Frankel (2016) [3], which produces a shorter rise time and higher dynamic stress drop for the subevents than for the background slip. In the case of the Tohoku earthquake, this choice resulted in good agreement between simulated and observed spectra [3].

The strike and dip angle on each subfault was computed directly from the irregular slab geometry. To compute the slip azimuth, we used the direction of motion of the JdF plate with respect to the North American (NA) plate along the JdF plate boundary from the Global Strain Rate Model (GSRM v 2.1) [33]. This results in a slip direction between 35° and 55° along the JdF-NA plate boundary as a result of the clockwise rotation of the JdF plate [34]. Rake was computed by taking the difference between the local slip azimuth and strike direction, and adding a random component using a normal distribution with a standard deviation of 45°. We generated a suite of different slip realizations to investigate the variability of ground motions with source parameters.

4. Wave Propagation Simulation

We simulated wave propagation from the suite of source models using the AWP-ODC code, which uses an explicit finite difference formulation on a staggered grid that is fourth-order accurate in space and second-order accurate in time. AWP was originally developed by Olsen [35] for single-CPU computers and later optimized for multiple-CPU systems using MPI [36]. A modern, highly scalable version of AWP supporting GPU accelerators was introduced in 2013 [37] for kinematic sources. The latest release of the CPU and GPU versions of AWP support frequency-dependent viscoelastic attenuation [38] and Drucker-Prager plasticity [39].

Because the original implementation of AWP employs a spatially uniform (equidistant) grid over the entire computational domain, the higher-velocity material making up most of the computational domain is significantly overdiscretized in a typical scenario simulation. Nie et al. [40] developed a discontinuous mesh (DM) method for the 3D fourth-order staggered-grid FD scheme used by AWP. The DM method operates by exchanging wavefield information between media partitions discretized with two different grid spacings, which alleviates the problem of overdiscretization and improves efficiency. Recently WEDMI was implemented in the scalable GPU version of AWP, and the method was verified against uniform mesh solutions by simulating the M 5.1 La Habra earthquake.

The discontinuous mesh version of AWP (AWP-GPU-DM) was also used for the simulations presented here. We first verified the accuracy of the DM solution for the Cascadia scenarios by performing both a uniform and DM mesh solution for the same scenario (rupture model A). For the uniform mesh solution, a grid spacing of 100 m was used throughout the computational domain, resulting in a mesh size of 6,540x10,730x600 grid points. For the discontinuous mesh solution, the small grid interval of 100 m was only used in the uppermost 8 km, and a larger interval of 300 m was used for the rest of the domain; the resulting grid sizes were 6,540x10,728x80 grid points for the fine and 2,180x3,576x176 grid points for the coarse mesh. The uniform mesh solution required ~3.4 hours using 4,440 Kepler K20X GPUs on the OLCF Titan supercomputer, while the discontinuous mesh solution required 480 GPUs for ~7.3 hours. Use of the DM reduced the computational cost by a factor of 4.3 for a model depth of 60 km, while the savings are significantly larger if a model depth of 120 km is used.

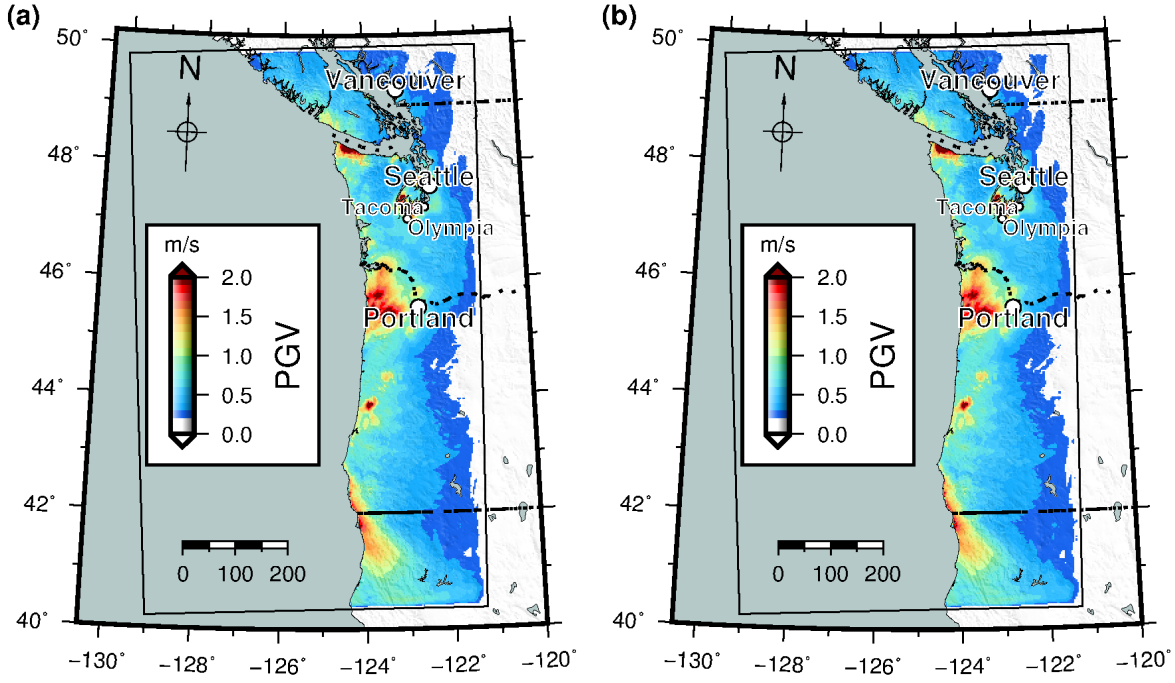

FIG. 4. Peak ground velocities (PGVs) from rupture scenario A' obtained with (a) uniform mesh and (b) discontinuous mesh method in AWP.

Peak ground velocities (PGVs) for rupture model A obtained with the discontinuous mesh FD method are very similar to those obtained from the uniform solution (FIG. 4). Because the sponge zones in the coarse grid contain less grid points than those in the fine or uniform grids, minor differences are expected close to the domain boundaries. Time series extracted at sites of interest also exhibit no notable difference between the two methods (FIG. 5).

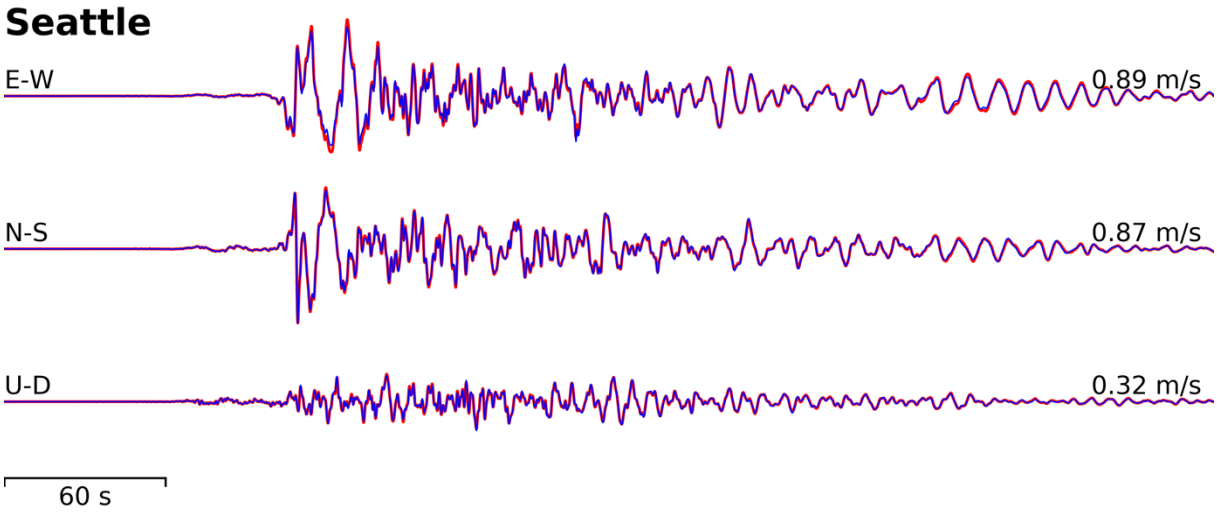

FIG. 5. Synthetic seismograms in downtown Seattle obtained from rupture model A' using uniform (thick red lines) and discontinuous (thin blue lines) mesh solutions. Numbers above traces indicate peak velocity.

5. Ground Motion Simulation Results

We simulated ground motions for four different realizations of background slip distributions (A, B, C and D). For the slip distribution in rupture model A, we also varied the location of subevents, the depth extent of the model and the response of near-surface sediments (linear vs. nonlinear) to analyze the sensitivity of ground motions to these parameters. Slip distribution D was used in two different hypocenter locations to study effects of rupture propagation direction.

TABLE 1: SIMULATED GROUND MOTIONS IN SEATTLE, VANCOUVER AND PORTLAND FROM DIFFERENT SLIP REALIZATIONS AND MODEL VARIATIONS

Site	Seattle				Vancouver				Portland			
Scenario	PGV (m/s)	SA (m/s²)			PGV (m/s)	SA (m/s²)			PGV (m/s)	SA (m/s²)		
		5s	2s	1.5s		5s	2s	1.5s		5s	2s	1.5s
A	0.73	0.97	1.85	2.73	0.25	0.48	1.04	1.76	0.43	0.37	2.03	4.39
A+	0.83	0.97	1.87	2.66	0.35	0.49	1.21	1.81	0.45	0.37	2.01	4.53
A++	0.85	0.99	1.83	2.62	0.35	0.50	1.13	1.79	0.45	0.37	2.00	4.62
A’	1.00	2.09	3.57	3.81	0.31	0.49	1.02	1.62	0.96	0.81	5.37	9.39
Ap	0.72	0.92	1.86	2.56	0.25	0.46	1.00	1.65	0.43	0.35	2.01	4.33
B	0.79	1.77	2.86	3.44	0.34	0.69	1.15	1.26	0.47	0.63	1.75	4.22
Dn	0.60	1.28	1.75	2.55	0.32	0.47	1.33	1.21	0.24	0.29	1.35	1.79
Ds	0.86	1.76	3.10	3.42	0.54	0.77	1.35	1.56	0.29	0.31	1.62	3.06

A+, A++: Slip distribution A using maximum domain depths of 120 km and 240 km, respectively

A’: Slip distribution A with subevents moved ~75 km to the east

Ap: Slip distribution B simulated with Drucker-Prager plasticity in near-surface sediments

Dn, Ds: Slip distribution D rupturing from north to south and south to north, respectively (120 km domain depth)

5.1. Influence of model depth

Ground motions obtained from slip distribution A with the shallow model (60 km maximum depth) reach 0.73 m/s in the Seattle and 0.25 m/s in the Vancouver downtown areas (FIG. 6a and Table 1). If the model depth is increased to 120 km (rupture model A+), PGVs increase to 0.83 and 0.35 m/s in Seattle and Vancouver, respectively (FIG. 6b Table 1). The depth of the model also increases simulated spectral accelerations (SAs) in Vancouver, but does not affect PGVs or SAs in Portland (Table 1). This suggests that ground motions are enhanced by the impedance contrast between the continental crust and the subducted slab beneath the Vancouver and Seattle regions, where the depth of the upper slab boundary exceeds 60 km (FIG. 1). Increasing the domain size to 240 does not lead to significantly different ground motion prediction compared to using 120 km (model A++ in Table 1).

5.2. Sensitivity of Ground Motions to Subevent Location

Because seismic waves in the frequency band relevant for buildings are emitted mostly by the subevents, the location of subevents is an important factor controlling the ground motions.

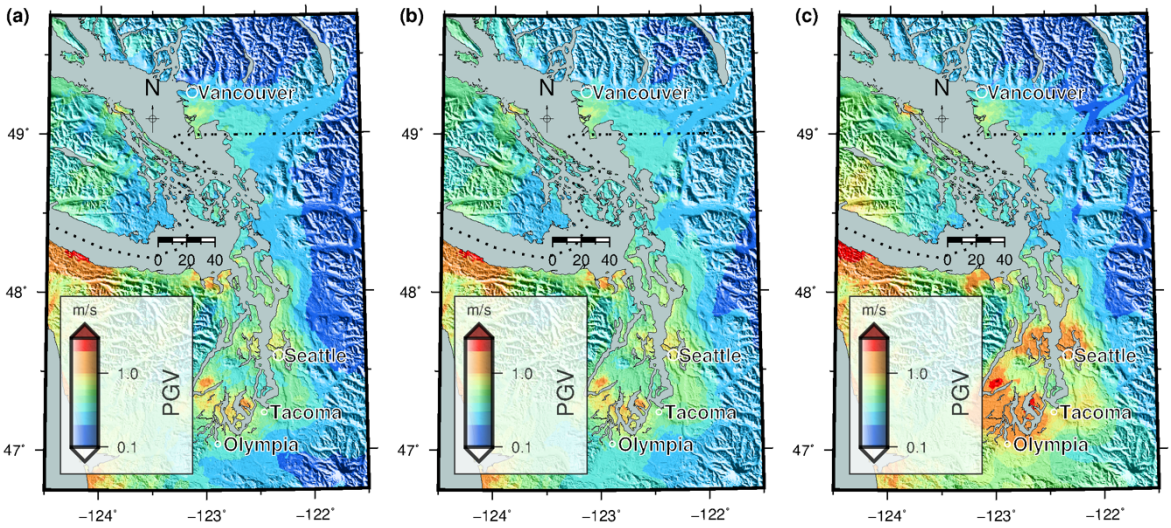

FIG. 6. PGVs in the Seattle and Vancouver areas from (a) rupture model A with 60 km domain depth, (b) A+ with 120 km domain depth and (c) A' with subevents moved ~75 km to the east.

FIG. 6c shows peak ground velocities in the Seattle and Vancouver areas obtained in rupture model A', which uses the same background and subevent slip distributions as model A, but with the subevents moved ~75 km to the east. Because this shift puts the urban centers of Seattle, Tacoma and Olympia closer to the second northernmost subevent (FIG. 3c), it results in larger ground motions in these areas (FIG. 6c), with PGVs above 1 m/s obtained in downtown Seattle (Table 1). Although we consider the subevent locations to be more realistic in rupture model A (e.g., rupture contained mostly in the transition and locked zones) than in model A', the sensitivity of ground motions to the subevent location is important, and it underlines the need to better understand and predict the depth-varying rupture properties of subduction zone earthquakes.

5.3. Plastic Yielding in Sedimentary Basins

Although nonlinear effects are usually considered to be important only at high frequencies ($f >$ 1 Hz), some studies suggest that they may also affect long-period surface waves [41, 42]. To assess if this nonlinearity would affect long-period ground motions in Cascadia during a megathrust event, we simulated the ground motion from slip distribution A inside a medium governed by Drucker-Prager plasticity (referred to as simulation Ap in Table 1). We only considered nonlinear effects in the shallow crust where the shear-wave velocity v_s is smaller than 2,000 m/s. We assumed a friction angle of 30° and a cohesion of zero for mesh points with shear-wave velocities below 750 m/s. For nodes with 750 m/s $\le v_s \le$ 2,000 m/s, we used the Hoek-Brown failure criterion [43] to predict the yield stress for a moderately fractured sandstone at the given depth. We then computed equivalent friction angles and cohesions pertaining to the Hoek-Brown failure stress, which were used to evaluate the Drucker-Prager yield condition in AWP [44, 45]. For simplicity we assumed isotropic stress conditions and a water table located at the surface.

FIG. 7a shows the principal plastic strain at the surface obtained from the nonlinear scenario Ap. Large deformations occur in the deep sediments of the Seattle basin and the Fraser river delta south of Vancouver. However, the plastic behavior of these sediments does not significantly affect ground motions at the frequencies considered here ($f \le$ 1.25 Hz), and the difference between the linear scenario A and the nonlinear scenario Ap only exceeds 10% in isolated areas (FIG. 7b) and is almost negligible for the sites considered in Table 1. We cannot

exclude that the absence of nonlinear effects is a consequence of enforcing a minimum shear-wave velocity of 625 m/s throughout the medium. The importance of plastic effects should be reassessed using higher-resolution 3D simulations, which would be able to include Holocene sediments with $v_s < 625$ m/s, which are encountered especially in the south Greater Vancouver area [2, 13], and in the Seattle basin.

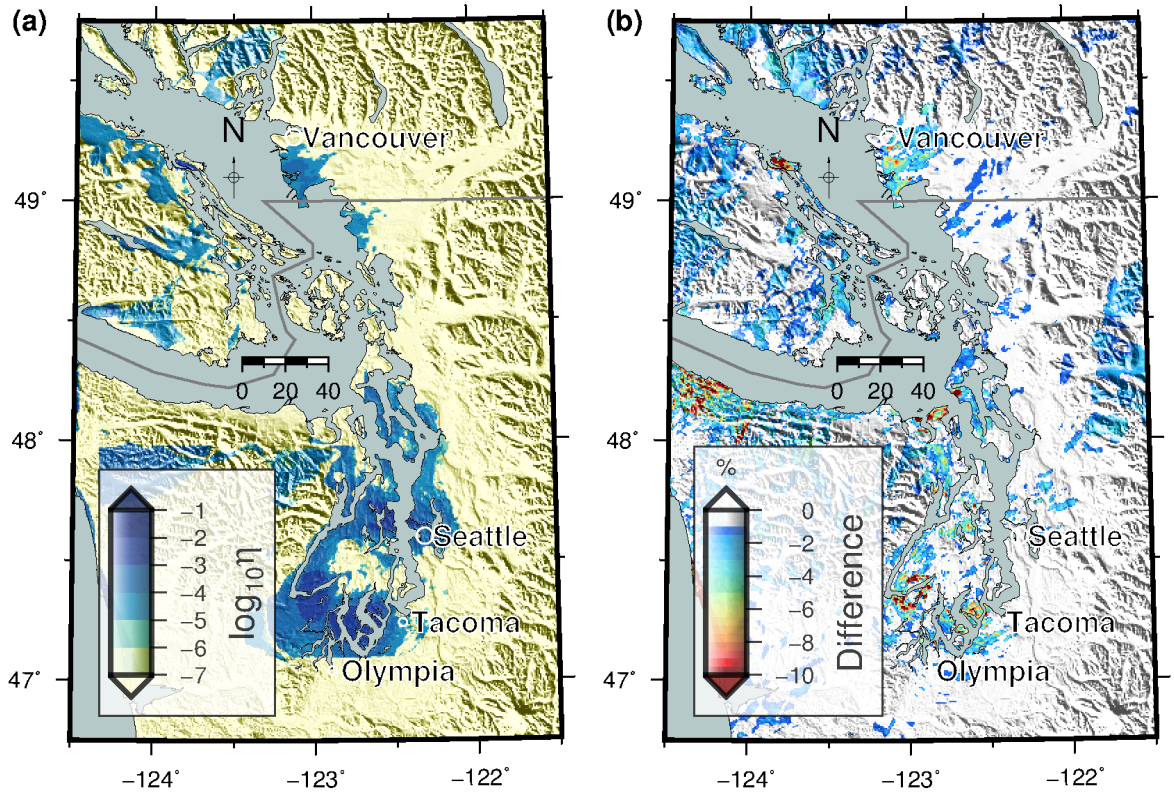

FIG. 7. Simulation of scenario Ap (rupture model A with Drucker-Prager plasticity). (a) Permanent plastic strain and (b) difference in PGV with respect to linear scenario A in Vancouver-Seattle areas.

5.4. Effect of Rupture Propagation Direction

Finally, we investigate how the rupture propagation direction would affect ground motions in the Seattle and Vancouver regions. FIG. 8 compares PGVs obtained from rupture scenario Dn, propagating from north to south, with scenario Ds, propagating from south to north. The direction of rupture propagation completely changes the distribution of PGVs especially in the northern half of the map. In rupture scenario Ds, PGVs exceed 1 m/s south of Vancouver and in the Seattle area, but they remain below 1 m/s in scenario Dn.

The pattern of 2s-SAs, on the other hand, exhibits less sensitivity to the direction of rupture propagation (FIG. 9), and 2s-SAs above 2 m/s^2 are predicted south of Vancouver and in the Seattle region for both scenario Dn and Ds. This observation indicates that effects of rupture propagation direction are frequency-dependent, as expected from source directivity effects.

Simulated seismograms in Vancouver are dominated by long-period ($T \approx 10$ s) phases arriving after approximately 150 seconds in scenario Ds (FIG. 10), but not in scenario Dn. These long-period wavetrains, emitted from the background slip and enhanced by effects of source directivity, control the large PGVs obtained in scenario Ds, while the PGVs are controlled by shorter-period arrivals from the subevents in scenario Dn. Maximum Fourier

amplitude spectra of the simulated velocity in Vancouver and Seattle (FIG. 11) occur at ~0.08 Hz for both scenario Dn and Ds, but with a much higher peak amplitude in scenario Ds than in scenario Dn. At frequencies above approximately 0.4 Hz, the spectra become insensitive to the rupture propagation direction.

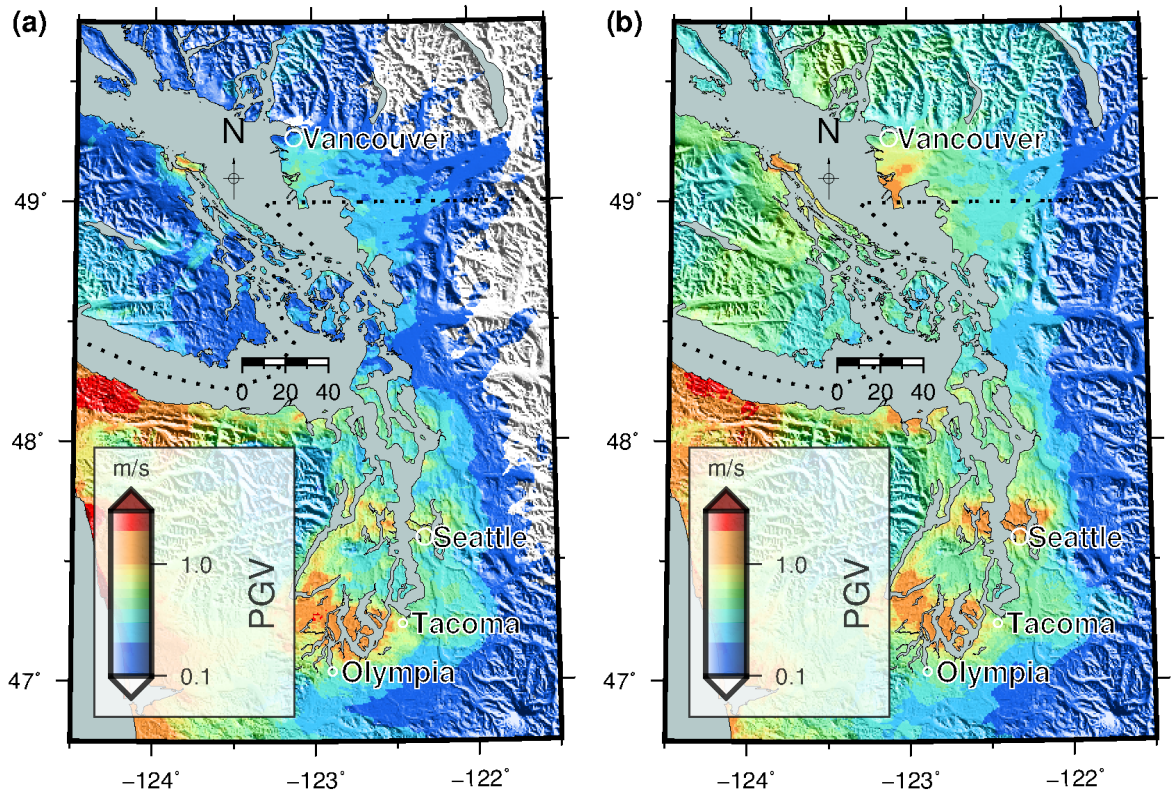

FIG. 8. PGVs from (a) scenario Dn rupturing from north to south, and (b) scenario Ds rupturing from south to north.

This frequency-dependency suggests that effects of source directivity are important at long periods (>10s), where constructive interference enhances the amplitude of long wavelengths emitted by the background slip in the direction of rupture propagation. However, the lack of a clear directivity effect at higher frequencies indicates that the short-period wavefronts emitted from the subevents are not coherent enough to give rise to constructive interfence.

6. Summary

We have carried out wave propagation simulations for a suite of M9 megathrust scenarios in the Cascadia subduction zone. An integrated and expanded velocity model of the region was generated by incorporating a local, higher-resolution model of the Georgia basin [13] into the larger Cascadia CVM [1], and extending the model to larger depth. We have generated an ensemble of kinematic source models, each composed of a background slip distribution with long rise time and superimposed subevents with short rise time to mimic the frequency-varying rupture properties observed in past subduction zone earthquakes [17]. In addition to simulating four different realizations of background and subevent slip distributions, we considered variations within these rupture models to study the sensitivity of ground motions to subevent location, computational domain depth, plastic yielding in near-surface sediments and rupture directivity effects.

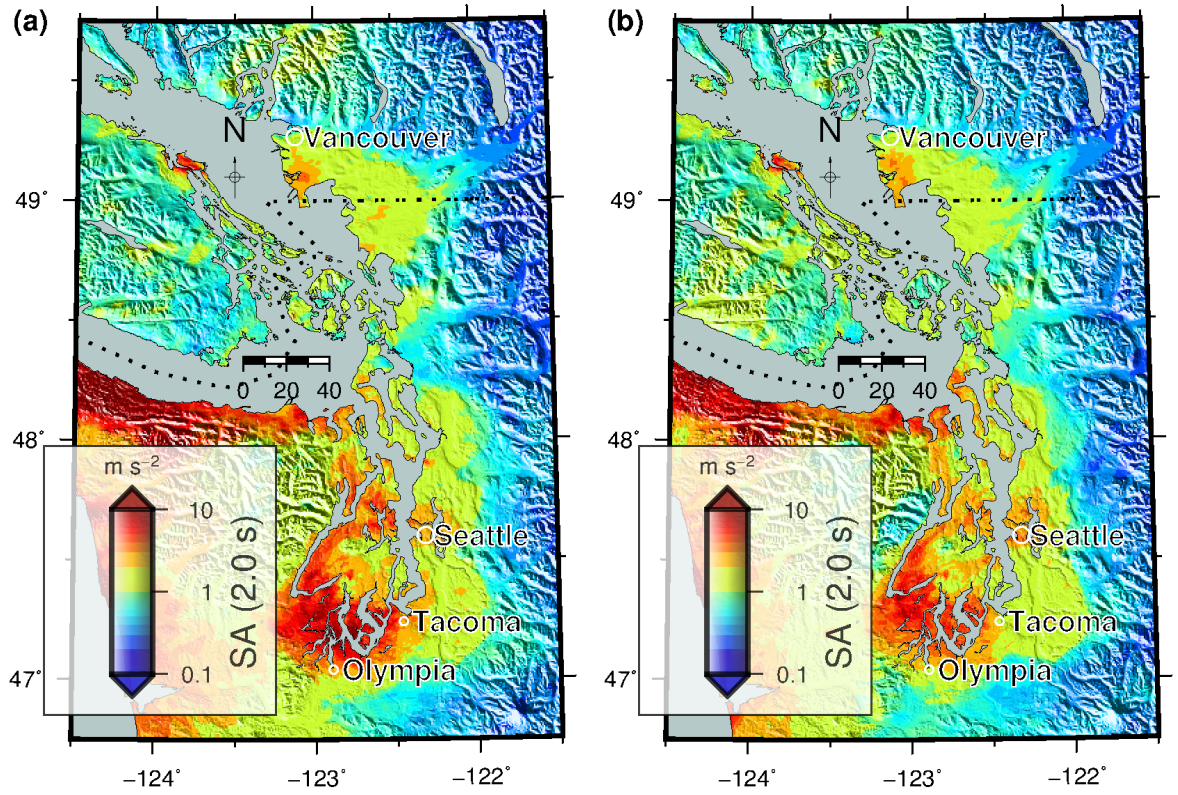

FIG. 9. 2s-SAs from model D rupturing (a) from north to south (Dn) and (b) from south to north (Ds).

Simulations were carried out using the discontinuous mesh version of the AWP finite difference code, which was verified against a uniform mesh solution for one of our rupture scenarios. Peak ground velocities range between 0.72 and 1.00 m/s in downtown Seattle and between 0.25 and 0.54 m/s in downtown Vancouver, where spectral accelerations at 2 s range between 1.75 and 3.75 m/s^2 and 1.04 and 1.35 m/s^2, respectively.

In the northeastern corner of the computational domain including Vancouver, where the depth of the subducting slab exceeds 60 km, higher PGVs are obtained if the computational domain is extended to 120 km, compared to a simulation performed with a mesh of 60 km depth defined in the Pacific Northeast CVM V1.6. Ground motions in Seattle are sensitive to the location of subevents, which control the shaking in the frequency range relevant for buildings ($f > 0.1$ Hz). Effects of Drucker-Prager plasticity are not important at frequencies below 1.25 Hz if shear-wave velocities are clipped at 625 m/s, even though the yield stress of near-surface sediments is exceeded in the Seattle basin and in southern Vancouver.

Effects of rupture directivity are important at the long periods emitted by the background slip distribution, and long-period wavetrains emitted in the direction of rupture propagation may lead to large PGVs in the Seattle and Vancouver areas. This rupture direction effect was not observed at frequencies above ~0.4 Hz. Future simulations should consider different variations in the rupture time of the subevents to corroborate this frequency-dependence of rupture directivity effects.

Because synthetic ground motions generated by our FD simulations are limited to frequencies below 1.25 Hz, a broadband method is used to predict ground motions for the entire frequency range of engineering interest (0—20 Hz). The SDSU broadband module has recently been adapted to predict broadband synthetics for large subduction zone earthquakes, and ongoing efforts include validating simulations against seismic data from the Tohoku earthquake.

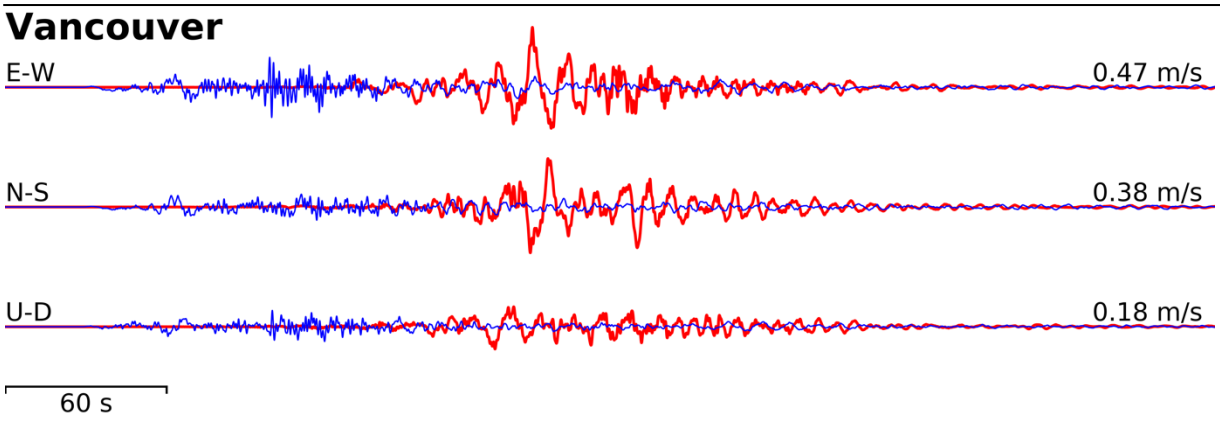

FIG. 10. Simulated ground motion in downtown Vancouver for scenario Dn rupturing from north to south (thin blue lines) and scenario Ds rupturing from south to north (thick red lines).

FD simulations currently in preparation will further reduce the grid spacing and use additional grid resolutions for increased efficiency. The minimum shear-wave velocity will be reduced to more realistic values and a geotechnical layer will be added to the Cascadia CVM in order to include realistic near-surface velocities.

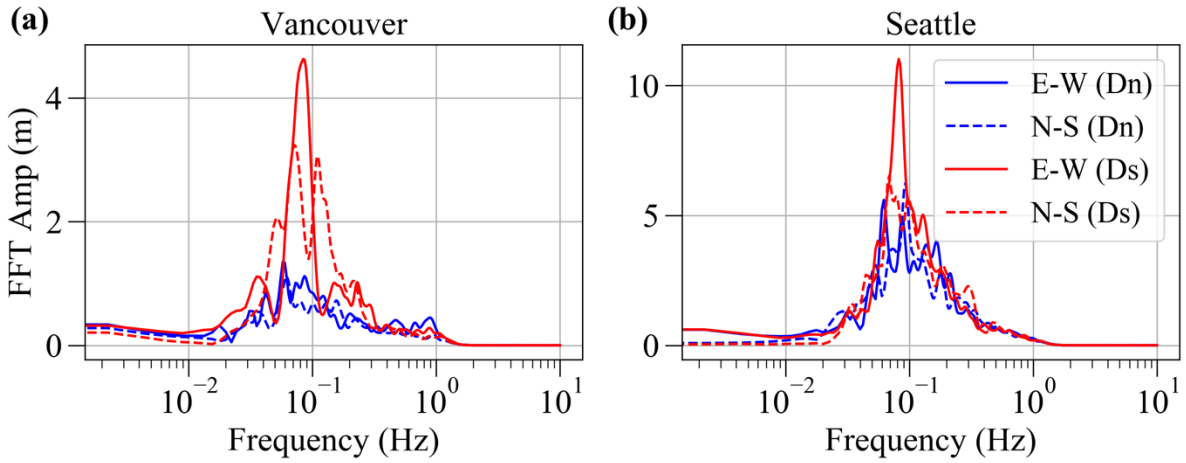

FIG. 11. Fourier amplitude of simulated velocities in (a) Vancouver and (b) Seattle from scenarios Dn (rupture from north to south) and Ds (rupture from south to north).

ACKNOWLEDGEMENTS

The authors thank Bill Stephenson for providing the Cascadia CVM and Sheri Molnar for providing the Georgia Basin velocity model. The Juan de Fuca slab geometry [8] was obtained from the USGS [46]. The tomography model [15] was downloaded from IRIS [47]. The global strain rates from GSRM v 2.1 [33] and plate boundaries were obtained from the UNAVCO PLATE motion calculator [48].

The authors acknowledge the Office of Science of the U.S. Department of Energy (DOE) for providing HPC resources that have contributed to the research results reported within this paper through an Innovative and Novel Computational Impact on Theory and Experiment (INCITE) program allocation award. Wave propagation simulations using AWP-GPU-DM were carried out on Titan, which is part of the Oak Ridge Leadership Facility at the Oak Ridge National Laboratory supported by DOE contract DE-AC05-00OR22725.

The authors thank the Willis Research Network (WRN) for funding this work.

REFERENCES

[1] W. J. Stephenson, N. G. Reitman, and S. J. Angster, "P-and S-wave Velocity Models Incorporating the Cascadia Subduction Zone for 3D Earthquake Ground Motion Simulations—Update for Open-File Report 2007–1348," US Geological Survey2331-1258, 2017.

[2] S. Molnar, "Predicting earthquake ground shaking due to 1D soil layering and 3D basin structure in SW British Columbia, Canada," 2011.

[3] A. Frankel, "Modeling Strong‐Motion Recordings of the 2010 M w 8.8 Maule, Chile, Earthquake with High Stress‐Drop Subevents and Background Slip," *Bulletin of the Seismological Society of America,* vol. 107, no. 1, pp. 372-386, 2017.

[4] T. H. Heaton and S. H. Hartzell, "Source characteristics of hypothetical subduction earthquakes in the northwestern United States," *Bulletin of the Seismological Society of America,* vol. 76, no. 3, pp. 675-708, 1986.

[5] R. S. Ludwin *et al.*, "Dating the 1700 Cascadia earthquake: Great coastal earthquakes in native stories," *Seismological Research Letters,* vol. 76, no. 2, pp. 140-148, 2005.

[6] A. Frankel, W. Stephenson, and D. Carver, "Sedimentary Basin Effects in Seattle, Washington: Ground-Motion Observations and 3D Simulations," *Bulletin of the Seismological Society of America,* vol. 99, no. 3, pp. 1579-1611, 2009.

[7] J. F. Cassidy and G. C. Rogers, "Variation in ground shaking on the Fraser River delta (Greater Vancouver, Canada) from analysis of moderate earthquakes," in *Proceedings of the 13th World Conference on Earthquake Engineering*, 2004, p. 1010.

[8] J. L. Blair, P. McCrory, D. Oppenheimer, and F. Waldhauser, "A geo-referenced 3D model of the Juan de Fuca slab and associated seismicity," US Geological Survey2327-638X, 2011.

[9] P. A. McCrory, J. L. Blair, F. Waldhauser, and D. H. Oppenheimer, "Juan de Fuca slab geometry and its relation to Wadati‐Benioff zone seismicity," *Journal of Geophysical Research: Solid Earth,* vol. 117, no. B9, 2012.

[10] K. B. Olsen, W. J. Stephenson, and A. Geisselmeyer, "3D crustal structure and long-period ground motions from a M9.0 megathrust earthquake in the Pacific Northwest region," *Journal of Seismology,* vol. 12, no. 2, pp. 145-159, 2008.

[11] S.-C. Han, C. Shum, M. Bevis, C. Ji, and C.-Y. Kuo, "Crustal dilatation observed by GRACE after the 2004 Sumatra-Andaman earthquake," *Science,* vol. 313, no. 5787, pp. 658-662, 2006.

[12] W. J. Stephenson, "Velocity and density models incorporating the Cascadia Subduction Zone for 3D earthquake ground motion simulations," Geological Survey (US)2331-1258, 2007.

[13] S. Molnar, J. F. Cassidy, K. B. Olsen, S. E. Dosso, and J. He, "Earthquake ground motion and 3D Georgia basin amplification in southwest British Columbia: Deep Juan de Fuca plate scenario earthquakes," *Bulletin of the Seismological Society of America,* vol. 104, no. 1, pp. 301-320, 2014.

[14] T. M. Brocher, "Empirical relations between elastic wavespeeds and density in the Earth's crust," *Bulletin of the seismological Society of America,* vol. 95, no. 6, pp. 2081-2092, 2005.

[15] C. Chai, C. J. Ammon, M. Maceira, and R. B. Herrmann, "Inverting interpolated receiver functions with surface wave dispersion and gravity: application to the western US and adjacent Canada and Mexico," *Geophysical Research Letters,* vol. 42, no. 11, pp. 4359-4366, 2015.

[16] D. Wang and J. Mori, "Frequency‐dependent energy radiation and fault coupling for the 2010 Mw8. 8 Maule, Chile, and 2011 Mw9. 0 Tohoku, Japan, earthquakes," *Geophysical Research Letters,* vol. 38, no. 22, 2011.

[17] T. Lay *et al.*, "Depth‐varying rupture properties of subduction zone megathrust faults," *Journal of Geophysical Research: Solid Earth,* vol. 117, no. B4, 2012.

[18] A. Frankel, "Rupture history of the 2011 M 9 Tohoku Japan earthquake determined from strong‐motion and high‐rate GPS recordings: Subevents radiating energy in different frequency bands," *Bulletin of the Seismological Society of America,* vol. 103, no. 2B, pp. 1290-1306, 2013.

[19] Y. Hayashi, H. Tsushima, K. Hirata, K. Kimura, and K. Maeda, "Tsunami source area of the 2011 off the Pacific coast of Tohoku Earthquake determined from tsunami arrival times at offshore observation stations," *Earth, planets and space,* vol. 63, no. 7, p. 54, 2011.

[20] W. Suzuki, S. Aoi, H. Sekiguchi, and T. Kunugi, "Rupture process of the 2011 Tohoku-Oki mega-thrust earthquake (M9.0) inverted from strong-motion data," *Geophys. Res. Lett.,* vol. 38, p. L00G16, 2011.

[21] D. Roten, H. Miyake, and K. Koketsu, "A Rayleigh wave back‐projection method applied to the 2011 Tohoku earthquake," *Geophysical Research Letters,* vol. 39, no. 2, 2012.

[22] D. Wang and J. Mori, "Rupture process of the 2011 off the Pacific coast of Tohoku Earthquake (Mw 9.0) as imaged with back-projection of teleseismic P-waves," *Earth Planets Space,* vol. 63, pp. 603--607, 2011.

[23] K. D. Koper, A. R. Hutko, T. Lay, C. J. Ammon, and H. Kanamori, "Frequency-dependent rupture process of the 2011 M w 9.0 Tohoku Earthquake: Comparison of short-period P wave backprojection images and broadband seismic rupture models," *Earth, planets and space,* vol. 63, no. 7, p. 16, 2011.

[24] B. Delouis, J. M. Nocquet, and M. Vallée, "Slip distribution of the February 27, 2010 Mw= 8.8 Maule earthquake, central Chile, from static and high‐rate GPS, InSAR, and broadband teleseismic data," *Geophysical Research Letters,* vol. 37, no. 17, 2010.

[25] S. Kurahashi and K. Irikura, "Source model for generating strong ground motions during the 2011 off the Pacific coast of Tohoku Earthquake," *Earth, planets and space,* vol. 63, no. 7, p. 11, 2011.

[26] S. Kurahashi and K. Irikura, "Short‐period source model of the 2011 M w 9.0 Off the Pacific Coast of Tohoku earthquake," *Bulletin of the Seismological Society of America,* vol. 103, no. 2B, pp. 1373-1393, 2013.

[27] P. Galvez, L. A. Dalguer, J. P. Ampuero, and D. Giardini, "Rupture Reactivation during the 2011 M w 9.0 Tohoku Earthquake: Dynamic Rupture and Ground‐Motion Simulations," *Bulletin of the Seismological Society of America,* vol. 106, no. 3, pp. 819-831, 2016.

[28] P. M. Mai and G. C. Beroza, "A spatial random field model to characterize complexity in earthquake slip," *Journal of Geophysical Research: Solid Earth,* vol. 107, no. B11, 2002.

[29] E. A. Wirth, A. D. Frankel, and J. E. Vidale, "Evaluating a Kinematic Method for Generating Broadband Ground Motions for Great Subduction Zone Earthquakes: Application to the 2003 Mw 8.3 Tokachi‐Oki EarthquakeEvaluating a Kinematic Method for Generating Broadband Ground Motions," *Bulletin of the Seismological Society of America,* vol. 107, no. 4, pp. 1737-1753, 2017.

[30] D. Roten, K. Olsen, J. Pechmann, V. Cruz-Atienza, and H. Magistrale, "3D simulations of M 7 earthquakes on the Wasatch fault, Utah, Part I: Long-period (0–1 Hz) ground motion," *Bulletin of the Seismological Society of America,* vol. 101, no. 5, pp. 2045-2063, 2011.

[31] R. Hyndman and K. Wang, "The rupture zone of Cascadia great earthquakes from current deformation and the thermal regime," *Journal of Geophysical Research: Solid Earth,* vol. 100, no. B11, pp. 22133-22154, 1995.

[32] M. Guatteri, P. M. Mai, G. C. Beroza, and J. Boatwright, "Strong ground-motion prediction from stochastic-dynamic source models," *Bulletin of the Seismological Society of America,* vol. 93, no. 1, pp. 301-313, 2003.

[33] C. Kreemer, G. Blewitt, and E. C. Klein, "A geodetic plate motion and Global Strain Rate Model," *Geochemistry, Geophysics, Geosystems,* vol. 15, no. 10, pp. 3849-3889, 2014.

[34] D. S. Wilson, "Confidence intervals for motion and deformation of the Juan de Fuca plate," *Journal of Geophysical Research: Solid Earth,* vol. 98, no. B9, pp. 16053-16071, 1993.

[35] K. B. Olsen, "Simulation of three-dimensional wave propagation in the Salt Lake Basin," Department of Geology and Geophysics, University of Utah, 1994.

[36] Y. Cui *et al.*, "Scalable earthquake simulation on petascale supercomputers," in *High Performance Computing, Networking, Storage and Analysis (SC), 2010 International Conference for*, 2010, pp. 1-20: IEEE.

[37] Y. Cui *et al.*, "Physics-based seismic hazard analysis on petascale heterogeneous supercomputers," in *Proceedings of the International Conference on High Performance Computing, Networking, Storage and Analysis*, 2013, p. 70: ACM.

[38] K. B. Withers, K. B. Olsen, and S. M. Day, "Memory-efficient simulation of frequency-dependent Q," *Bulletin of the Seismological Society of America,* vol. 105, no. 6, pp. 3129-3142, 2015.

[39] D. Roten *et al.*, "High-frequency nonlinear earthquake simulations on petascale heterogeneous supercomputers," in *Proceedings of the International Conference for High Performance Computing, Networking, Storage and Analysis*, 2016, p. 82: IEEE Press.

[40] S. Nie, Y. Wang, K. B. Olsen, and S. M. Day, "Fourth‐Order Staggered‐Grid Finite‐Difference Seismic Wavefield Estimation Using a Discontinuous Mesh Interface (WEDMI)," *Bulletin of the Seismological Society of America,* vol. 107, no. 5, pp. 2183-2193, 2017.

[41] W. B. Joyner, "Strong motion from surface waves in deep sedimentary basins," *Bulletin of the Seismological Society of America,* vol. 90, no. 6B, pp. S95-S112, 2000.

[42] D. Roten, K. Olsen, S. Day, Y. Cui, and D. Fäh, "Expected seismic shaking in Los Angeles reduced by San Andreas fault zone plasticity," *Geophysical Research Letters,* vol. 41, no. 8, pp. 2769-2777, 2014.

[43] E. Hoek, "Strength of rock and rock masses," *ISRM News Journal,* vol. 2, no. 2, pp. 4-16, 1994.

[44] D. Roten, K. Olsen, and S. Day, "Off‐fault Deformations and Shallow Slip Deficit from Dynamic Rupture Simulations with Fault Zone Plasticity," *Geophysical Research Letters,* 2017.

[45] D. Roten, K. Olsen, S. Day, and Y. Cui, "Quantification of fault-zone plasticity effects with spontaneous rupture simulations," *Pure and Applied Geophysics,* vol. 174, no. 9, pp. 3369-3391, 2017.

[46] USGS. (2011). *A Geo-Referenced 3D Model of the Juan de Fuca Slab and Associated Seismicity*. Available: https://pubs.usgs.gov/ds/633/

[47] IRIS. (2015). *Data Services Products: EMC-WUS-CAMH-2015 3D shear-wave velocity model of the western United States*. Available: https://ds.iris.edu/ds/products/emc-wus-camh-2015/

[48] UNAVCO. (2018). *Plate motion calculator*. Available: https://www.unavco.org/software/geodetic-utilities/plate-motion-calculator/plate-motion-calculator.html